



Optical images reveal the role of high temperatures in triggering the 2021 Chamoli landslide

Jing Tian¹, Wentao Yang^{1, 2}, Jian Fang³, Chong Xu⁴

¹Three-gorges reservoir area (Jinyun Mountain, Chongqing) Forest Ecosystem National Observation and Research Station, School of Soil and Water Conservation, Beijing Forestry University, Beijing 100083, PR China

²Academy of Plateau Science and Sustainability, People's Government of Qinghai Province and Beijing Normal University, Xining 810016, China

³College of Urban and Environmental Sciences, Central China Normal University, Wuhan, 430079, China

⁴National Institute of Natural Hazards, Ministry of Emergency Management of China, Beijing, 100085, China

10 *Correspondence to:* Wentao Yang (yang_wentao@bjfu.edu.cn)

Abstract. The 2021 Chamoli ice-rock landslide formed a landslide-flood hazard chain by claiming 200 lives and destroying two hydroelectric power plants. The reason for this landslide has been elusive due to difficulty in retrieving reliable deformation time series before the landslide. Here we proposed a histogram-based method to reconcile deformation inconsistencies measured in different optical sensors. We find the Chamoli ice-rock deformed >80 m from 2013 to 2021 with exceptionally high deformations in summers of 2017/18, which were related to high summer temperatures. Final collapse in February 2021 is also related to high temperature. Rising temperatures weakened shear strength of the ice on the sliding plane triggering the Chamoli landslide to move. With climate warming, more similar, hard to predict ice-rock landslides in deglaciating high mountains are inevitable, posing new challenges to local communities and beyond. Optical remote sensing images provide an indispensable data in deciphering early precursors of similar hazards.

20 1 Introduction

Landslides in deglaciating high Asia mountains are more disastrous to local communities than other environments (Shugar et al., 2021; Cook et al., 2018). Extremely high local relief of these deglaciating mountains means tremendous kinetic energy after slope collapses. These mountains are abundant of unvegetated, loose sediments (moraines), which are more erodible than low mountains (Gruber and Haeberli, 2007). Widespread and persistent warming of permafrost has been observed in polar regions and at high elevations since about 1980; trends in permafrost warming are consistent with trends in air temperature (Smith et al., 2022). Given the phenomenon of global warming, rising temperatures have led to rapid melting of glaciers, shrinking glacier cover, warmer permafrost, and deeper active layers, resulting in many cracks and U-shaped bedrock slopes that are unsupported and could collapse at any time (Biskaborn et al., 2019; Lacroix et al., 2022).

The changing climate should play a pivotal role in initiating landslides in these deglaciating high Asia mountains, yet direct observations at slope scale are scarce. Most existing works are regional analysis of the relationships between climate change and landslide inventory changes (Emberson et al., 2021; Pei et al., 2023; Kirschbaum et al., 2020) and in other parts of the



world (Deline et al., 2021; Coe et al., 2018; Lewkowicz and Way, 2019). However, these landslide inventories are mainly interpreted from relatively low elevations, where vegetations are abundant and landslides stand out distinctly from background ground features in remote sensing images (Larsen and Montgomery, 2012). In contrast, landslides in unvegetated, high deglaciating mountains are much more difficult to interpret and are therefore largely overlooked. Unfortunately, climate warming is elevation dependent, which means warming temperature has been disproportionately influencing higher than lower mountains (Mountain Research Initiative EDW Working Group 2015). Lack of observations hinder understanding of these processes and in particular its response to climate change (Sæmundsson et al., 2018). Most observations in high deglaciating mountains are in European. A recent work by Bast et al. (2024) with multiple in-situ methods found deceleration of an ice-rich rock glaciers was associated with low winter snowfall and cool summer temperatures. Their analysis did not consider changes of ice strength in the sliding zone, because cooler summer temperatures could increase ice strength leading to slower rock glacier deformation than warmer summers.

Recent disasters that originated from harsh, extremely high Asian mountains draw our attention to examine these slope stabilities beforehand (Shugar et al., 2021; Cook et al., 2018; Guo et al., 2020). The 7 February 2021 Chamoli landslide-flood hazard chain is such a prominent event. The ice-rock blocked failed from an elevation of ~5500 m to the bottom of the valley ~1800 m below (Shugar et al., 2021). Extremely high relative relief (~1800 m) of the block bear very high gravitational potential energy, which transformed to tremendous kinetic energy (Jiang et al., 2021). The ice-rock block smashed into the valley bottom and run a long distance entering the Ronti Gad–Rishiganga River confluence leading to a surged flood that destroyed two hydropower plants about 15km and 24 km far from the landslide source, claiming ~200 lives. Previous works showed clear precursors of > 10m horizontal displacements in the last few years (Qi et al., 2021; Van Wyk de Vries et al., 2022). However, observations on these deglaciating mountain environments are always challenging. First, deformations of similar magnitude (>10 m in 2~5 years) before landslides are beyond the capability of mainstream SAR interferometry (InSAR) measurements. Second, these extremely high mountain environments are very complex terrains frequently influenced by mountain shadows and snows. There are high uncertainties among different datasets and a lack of intra-annual deformation measures for the Chamoli landslide in previous studies hindering a holistic assessment of climate change's impact and the reason of the ice-rock collapse remains largely unknown (Qi et al., 2021; Van Wyk de Vries et al., 2022).

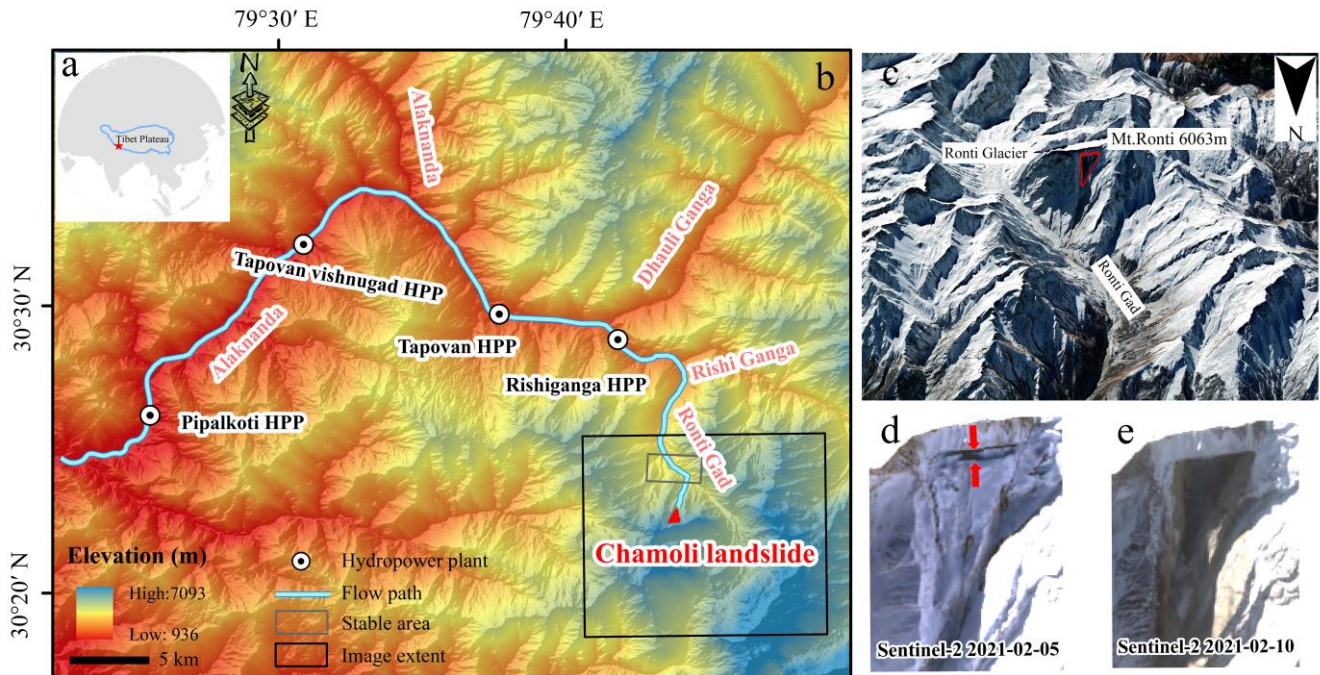
The aims of this work are 1) to reconcile deformation measures from different optical sensors, 2) to derive inter- and intra-annual deformations for the Chamoli ice-rock landslide, and 3) to disentangle mechanisms that lead to this landslide. Findings of this work would help understand hazard chain processes in deglaciating high mountain Asia.

60 **2 Study area**

On 7 February 2021, at 4:51 UTC [10:21am. Indian Standard Time (IST)], a catastrophic ice-rock landslide occurred in the Chamoli district of the North Arkhand, India (30.38°N, 79.75°E, 5000~5600 m). A large chunk of ice-rock (~27 × 10⁶ cubic



meters, Shugar et al., 2021) dislodged from the steep north face of the Ronti Peak at an altitude of about 5500 m (as shown in Fig. 1) and rapidly descended 1800 m reaching the bottom of the Gonti Gad valley, triggering a massive flood.



65

Figure 1: The study area is located on the southwest of the Tibet Plateau (a). ALOS 30m DEM topographic map (Provided by Japan Aerospace Exploration Agency) in (b) highlights the blue line, which was the travelling path of the hazard chain initiated by the landslide. The Rishiganga HPP (hydro power plants) and Tapovan HPP are two major affected infrastructures. The grey smaller rectangular in (b) is the stable area used in *Exp 1-3* in Table 1. (c) Location of the Chamoli landslide in the glacier (from © Google Earth 2024). (d to e) Pre-event and post-event satellite imagery of the site of the collapsed rock and glacier block, and the resulting scar. The red arrows in (d) indicate the fracture that became the headscarp of the landslide. Satellite imagery in (d) to (e) is from Sentinel-2 (Copernicus Sentinel Data)

70

This region is a tectonically active zone that is dominated by high relative relief glacial landform. It has rich permafrost. In many areas of the alpine environment, the past 50 years have seen a reduction in the amount of glacier cover, a rise in permafrost temperature, deeper active layers (Biskaborn et al., 2019). Many fissures have been created in permafrost locations as a result of rock/ice separating due to climate factors. There was no feelable earthquake in the region and around in the past ten years based on the USGS earthquake catalogue. The area is mainly composed of metamorphic rocks, which are dominated by mixed rock gneisses. The area around the destroyed Tapovan Vishnugad Hydropower Station is characterized by metasedimentary blueschist schist, quartzite, marble, gneiss and calc-silicates (Valdiya & Goel, 1983). Non-tectonic joints in layered bedrocks make it susceptible to glaciation and neotectonics (McColl, 2012; Sahoo et al., 2000). There are many types of natural hazards around the study area (e.g., flash floods, mudslides, landslides and earthquakes) (Bhambri et al., 2016). The climate of the region is characterized by warm humid summers and cold humid winters. The difference between the average monthly maximum and minimum temperatures is about 20°C, with the highest temperatures occurring in summer monsoon

80



months (Shrestha et al., 2021). Mean annual precipitation is more than 1,000 mm, two-thirds of which occurs in summer
85 months (June to September) brought by the southwest monsoon. Winter months (between November and March) precipitation
is brought by the western disturbances (Das et al., 2019).

3 Material and methods

3.1 Data

To detect the slope deformation that occurred before the landslide, we used the red band of the Sentinel-2 (10m resolution)
90 level-1C images referring to (Yang, 2020; Yang et al., 2020a, 2020b). We used the 15m resolution panchromatic band of the
Landsat 8 Tier 1 TOA reflectance images. We visually checked all Landsat 8 images in the Chamoli area and obtained 71 clear
images without clouds and haze from 2013 to 2021. As the Chamoli landslide is located on a north-facing slope, it is partially
or totally covered by mountain shadows in some periods of the year. Among these 71 clear Landsat 8 images, the landslide in
35 images is not affected by mountain shadows. Similarly, 43 clear Sentinel-2 images without mountain shadows from 2016
95 to 2021 were used in this work (Supplement 1). We used historical monthly temperature data from the European Centre for
Medium-Range Weather Forecasts (ECMWF) ERA5 dataset (Hersbach et al., 2023) from 1979 to 2020 to analyse the impacts
of temperature data on landslide deformations. The ERA5 in complex terrain (e.g., high mountain regions of Asia) has been
investigated in several studies and validated for several regions of HMAs (Khanal et al., 2023). Because the spatial resolution
of the ERA5 is much too coarse (0.25°), we used a nearest meteorological station that is available to us, ~170 km from the
100 landslide to validate the ERA5 temperature data (Supplement 3). We used NASA's monthly Global Precipitation
Measurements (GPM) data (Skofronick-Jackson et al., 2017) from 2013 to 2020 to investigate the effect of precipitation on
the landslide deformation.

3.2 Method

We can compare two optical images of different dates to derive deformation of the Chamoli landslide with pixel offset tracking
105 methods (POT). In this study, we first composed image pairs by selecting any two optical images with acquisition dates < 550d
from the same sensor. Second, we used the COSI-Corr (Co-Registration of Optically Sensed Images and Correlation, Leprince
et al., 2007; Li et al., 2024), a POT method to derive initial deformation values. Third, we used both the traditional stable area
method and our proposed histogram-based method to correct mismatches in image pairs during POT. From that, we derive
time series deformation of the landslide with the least square regression method as Zhang et al., (2022).

110 3.2.1 Mismatch correction in image pairs and the proposed histogram-based method

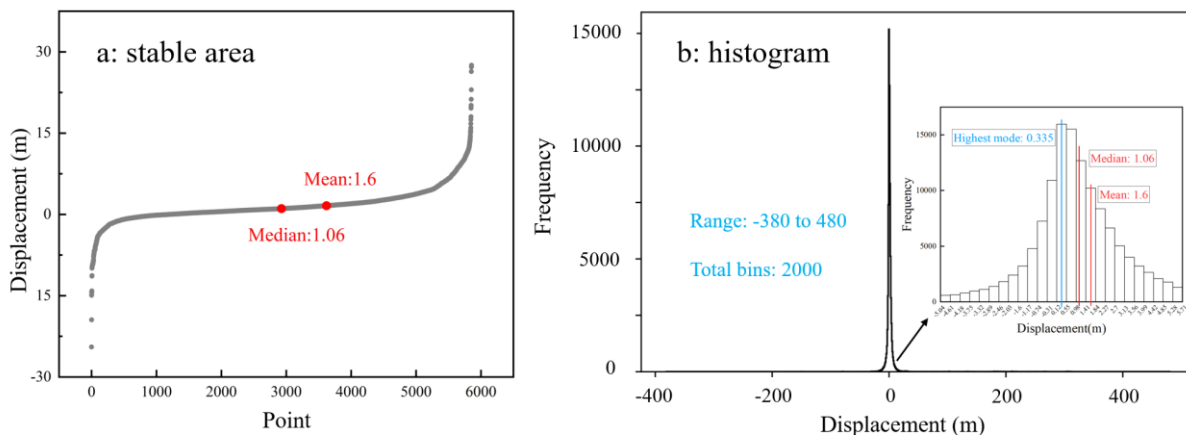
The COSI-Corr is a frequently used method to derive surface deformations between two optical images (Miles et al., 2021;
Chen et al., 2020; Michel et al., 2018). With the Fourier transformation, COSI-Corr utilizes two sliding (initial and final)
windows to consecutively detect differences in an image pair. In this work, the initial and final window sizes of the frequency



115 correlator are 64 and 32, respectively, consistent with Yang et al. (2020). The N/S (north/south), E/W (east/west) and SNR are
three output layers for a given image pair. Although registrations have been implemented in optical images, there are still sub-
pixel mismatches between any two images. It is a common way to remove mismatches in N/S and E/W layers from an image
pair by subtracting the mean or median (N/S and E/W) deformations in a selected stable area (Bontemps et al., 2018; Lacroix
et al., 2018; Yang et al., 2020). Mean or median values of the stable area are frequently used as approximations of the mismatch
value. Different stable areas should produce the same mismatch values for a given image pair. These estimated mismatch
120 values can be biased due to many factors. Firstly, selection of a stable area is always subjective and based on personal
experiences. It is even more challenging to select a stable area in topographic complex mountains like the Chamoli area.
Second, the size and location of stable areas can influence the mean or median values, as they can be easily biased by abnormal
POT results even constrained by the SNR signals (Bontemps et al., 2018). Biases in estimating mismatch values in image pairs
can propagate to deformation time series leading to inconsistencies among different image types.

125 To solve this problem, we first used all POT results from the entire study area to form a histogram with 2000 bins. Second, we
find the highest deformation frequency bin based on the assumption that the deformation of the study area follows a normal
distribution. Third, the mismatch value is estimated by the mean of the bin's (maximum and minimum) boundary as a mode
value. Finally, this mode value is eliminated as the mismatch between images in the given pair from POT results. This new
method does not need to select a stable area.

130 Here we selected the N/S layer of a POT result as an example to show the difference between the traditional stable area method
and our proposed histogram-based method. Fig. 2a shows that the mean value is 1.6 m, and the median value is 1.06 m in the
stable area (Gray rectangle in Fig. 2b). In traditional methods (such as the first three experiments in this work), either the mean
or the median values will be used as the mismatch between the two images in the image pair. To use our proposed method, we
created a histogram with 2000 bins, ranging from -380 to 480 m for the entire image (the area with POT result). Then, we
135 identify the bin with the highest deformation frequency (the column with the vertical blue line in the centre), and estimate the
mismatch value as 0.335 m by averaging the bin's (maximum and minimum) bounds (Fig. 2b).





140 **Figure 2: Average and median values within the stable area(a). The mean of the bin boundaries with the highest frequency is used as the mismatch in this image pair for the N/S layer(b). Note, the vertical blue line (inset b) is the values estimated from our proposed method and the two vertical red lines (inset b) were mean and median values used in traditional stable area method.**

3.2.2 Five experiments to reconcile measure inconsistencies

To test the performance of our proposed histogram-based method, we used five experiments in this study to derive deformation of the landslide (Table 1). We used a stable area (the grey rectangular in Fig. 1b) in the first three experiments, whereas the newly proposed histogram-based method is used for the last two experiments. In the first experiment, we used all 71 clear
 145 Landsat 8 images, some of which are covered by mountain shadows (i.e. Supplement 2 mountain shadows cover part or the entire Chamoli landslide). In the other four experiments, we selected Landsat 8 and Sentinel-2 images without mountain shadows from clear ones (Supplement 2). After correcting mismatches in image pairs, we used the same method as Zhang et al. (2022) to derive time-series deformation for the study area.

150 **Table 1. Five experiments in this work. These experiments were designed to test the performance of the proposed histogram-based method.**

Experiment No.	Data	Number of images	Number of pairs	Method
1 st	Landsat 8	71	897	Stable area with shadow images
2 nd	Landsat 8	35	209	Stable area & no shadow images
3 rd	Sentinel-2	43	495	Stable area & no shadow images
4 th	Landsat 8	35	209	histogram-based & no shadow images
5 th	Sentinel-2	43	495	histogram-based & no shadow images

POT needs two images of different dates to compare an image pair. In this work, any two images of the same type (Sentinel-2 or Landsat 8) with < 550 days interval are composed of an image pair (Supplement 1). With all 71 clear Landsat 8 images, there are 897 image pairs in the first experiment. By excluding 36 shadow Landsat 8 images, 209 image pairs are used in the second and fourth experiments. For the third and fifth experiments, 495 image pairs were composed with 43 Sentinel-2 images.
 155 Fig. 3 is a flowchart of the proposed method.

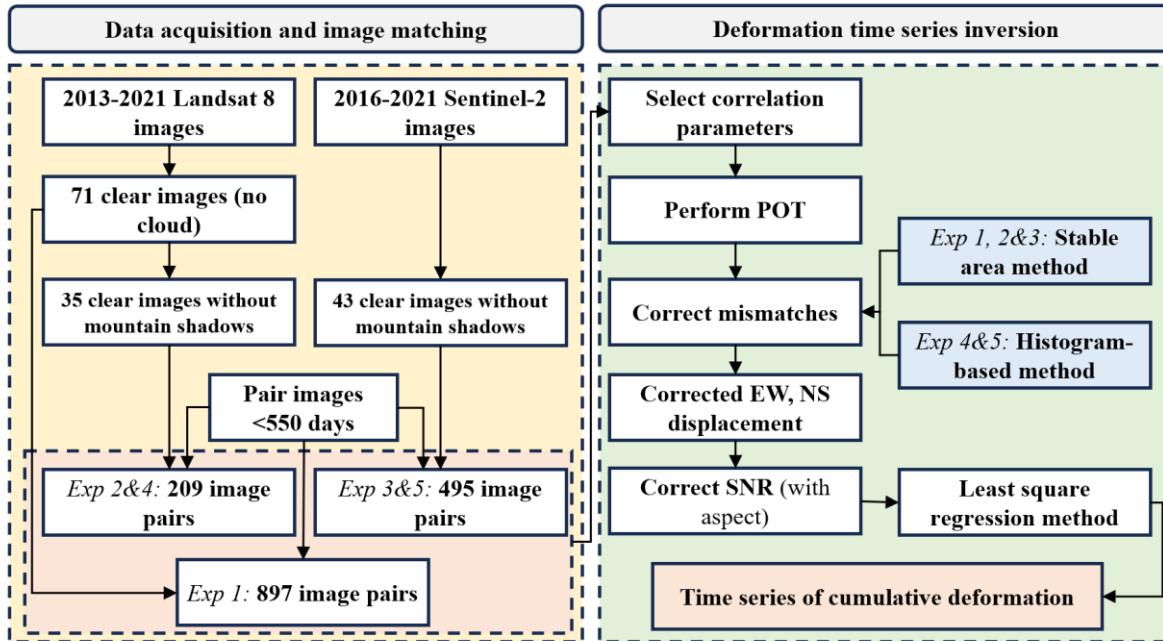
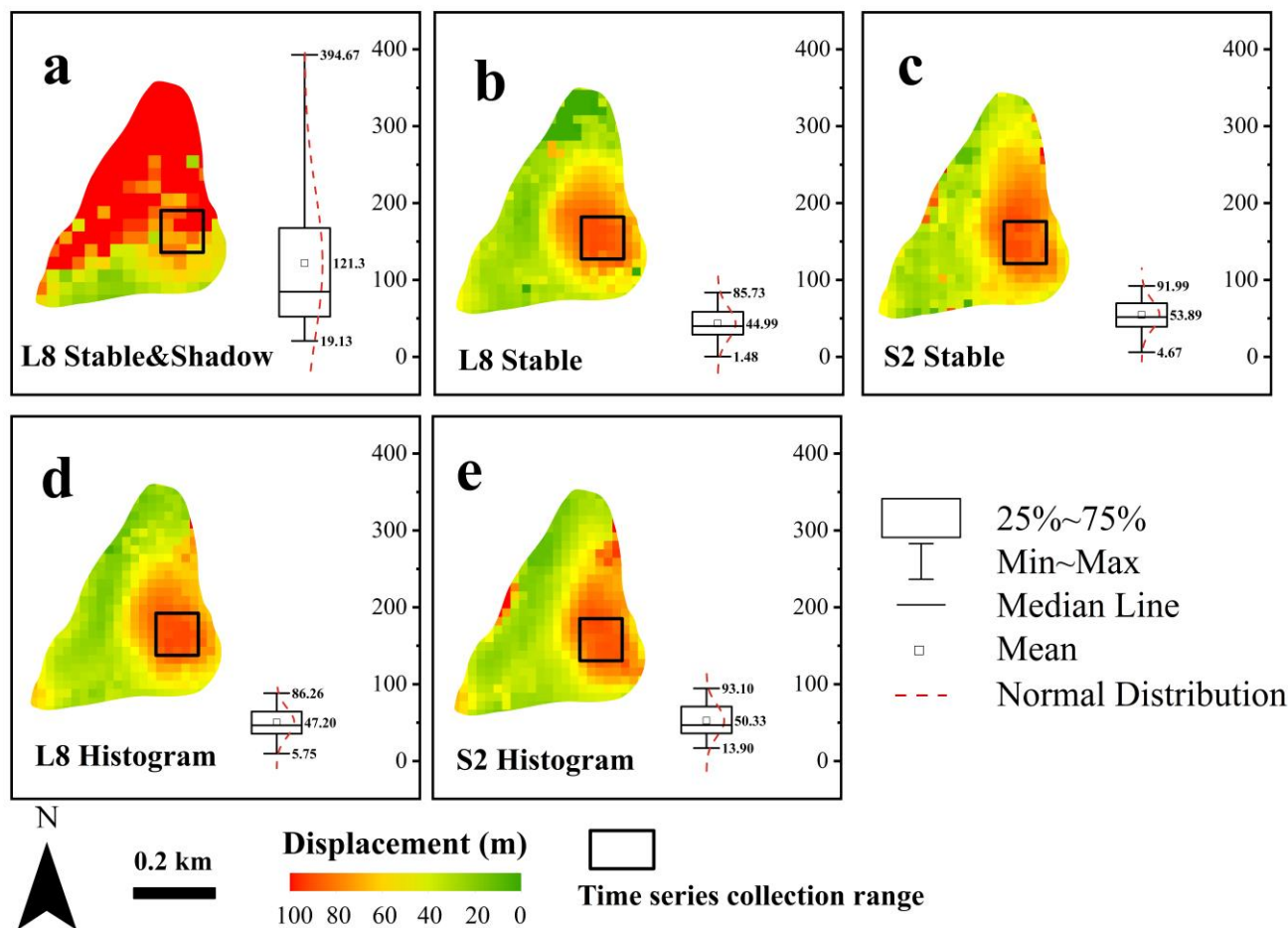


Figure 3: Flowchart of the proposed method.

4 Results

160 4.1 Reconciled Landsat 8 and Sentinel-2 measurements

Fig. 4 shows the derived deformation of the landslide before 2021 (the landslide failed in February 2021). Slope deformation in Fig. 4a (including images covered by mountain shadows) is different from the other four results. Clear images with mountain shadows in *Exp 1* seriously deteriorated deformation of the landslide in Fig. 4a. Spatial deformation patterns that did not use shadow images agree well with each other and unanimously show that the main deformation occurred at the east part of the landslide. Their spatial consistency can also be validated by their corresponding boxplots (embedded in Fig. 4). Using the traditional stable area method (*Exp 2 & 3*), the mean deformation difference between Landsat 8 (44.99 m, Fig. 4b) and Sentinel-2 (53.98 m, Fig. 4c) is ~9 m. In contrast, the proposed histogram-based method reduced this difference to < 5m (Landsat 8 with *Exp 4* mean is 47.20 and Sentinel-2 with *Exp 5* mean is 50.33, Fig. 4d & 4e).



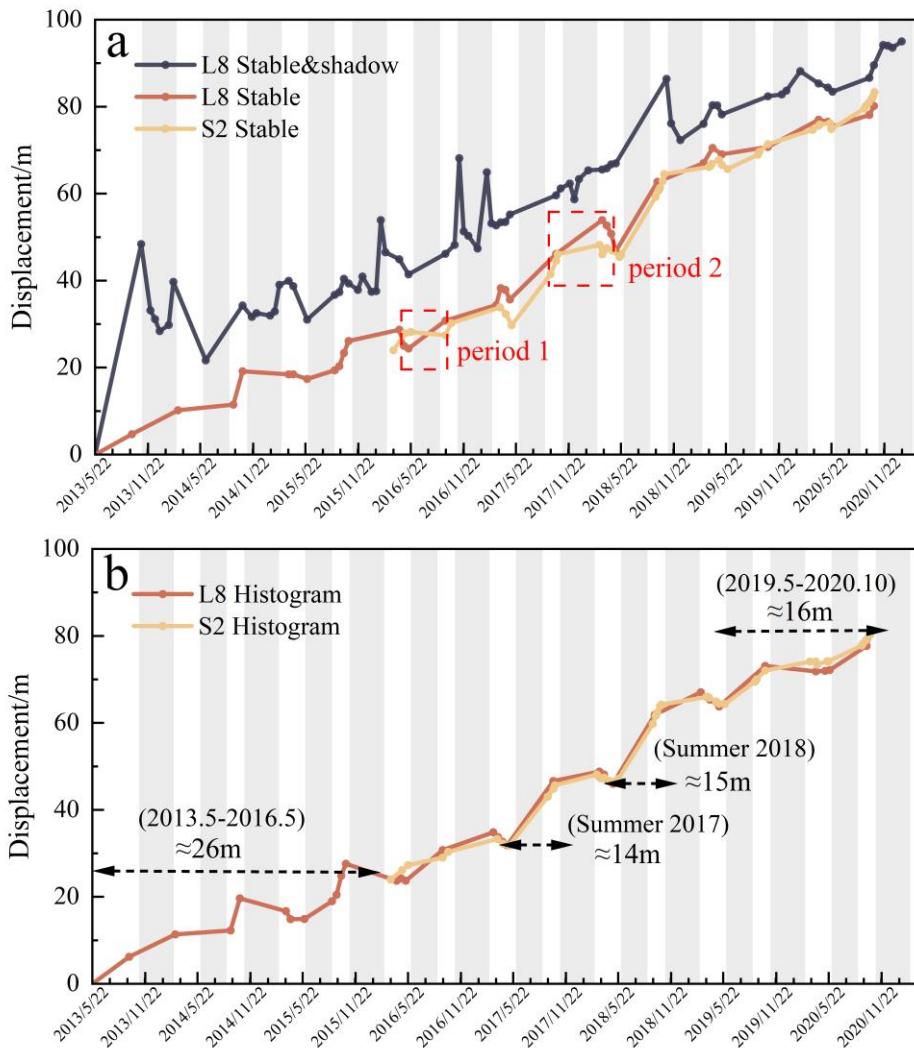
170 **Figure 4: Deformation results of the Chamoli landslide. Results in panels a-c are derived with stable area (Exp 1-3), whereas panels d-e used histogram-based method (Exp. 4-5). All 71 clear Landsat images were used in panel a. Results in panels b-c did not use shadow images. (Shadow images mean the Chamoli landslide is partially or totally covered by mountain shadows). The black polygons are used to derive deformation time-series in Fig 5. Panels a-e are embedded with boxplots of deformation with one- and three-quarter percentiles, range, mean and median values, the red dashed curves are fitted normal distributions.**

175 Fig. 5 shows the cumulative deformation time series from the five experiments in the east part of the landslide (the black polygons in Fig. 4). The deformation time series that uses all clear (including shadow-covered) Landsat 8 images and the stable area (the black dotted line in Fig. 5a) has very large sparks, which means very large uncertainties. In comparison, results (L8 stable and S2 stable in Fig. 5a) that excluded shadow images have much less sparks, meaning excluding shadow images could improve deformation time series. However, there are still inconsistencies between L8 stable and S2 stable results in the red dashed polygons in Fig. 5a (period 1 & 2). For example, L8 stable shows accelerated deformation, while S2 stable shows the deformation stagnated between April and September 2016 (period 1). Both measurements do not agree with each other on whether the deformation continued increasing between September 2017 and March 2018 (period 2).

180



By using our proposed histogram-based method, these temporal inconsistencies between Landsat 8 and Sentinel-2 data were reconciled (Fig. 5b). Both measurements show the deformations are much higher in the May-October periods in 2017 and 185 2018 than other years. The landslide moved ~ 33 m in the two-year period of 2017-2018. It moved about 14 m and 15 m in summers of 2017 and 2018, respectively. In contrast, the landslide moved approximately 26 m in three years from May 2013 to May 2016 and about 16 m over the last two years before collapse (2019.5-2020.10).



190 **Figure 5:** Deformation time-series of the east part of the landslide (black polygons in Fig. 4a-e). Deformation time-series for Fig. 4a-c (*Exp 1-3*) are shown in (a) and time-series for Fig. 4. d-e (*Exp 4-5*) are shown in (b). Note, inconsistencies in red dashed polygons between L8 stable and S2 stable results in (period 1 & 2 of a). Temporally consistent results in (b) show large accelerations in summers of 2017 and 2018.



4.2 Deformation accelerations in summers of 2017/18

To compare deformations of the Chamoli landslide in summers (4.1-9.30) and winters (10.1-3.31 the following year), we made
 195 simplified the deformation time series from 2013 to 2021 for the landslide and its neighbouring stable slopes. Each year,
 Sentinel-2 and Landsat 8 images acquired from early March to late October are not influenced by mountain shadows. By
 averaging time series of deformations derived from these two kinds of remote sensing images with the histogram-based method,
 we grouped deformations into summer and winter deformations (Fig. 6b). Neighbouring slopes remained very stable during
 the study period (Area III & IV in Fig. 6a & 6b). Though different parts of the landslide have distinct spatial deformations
 200 (mean displacement in Area I is ~80 m while in Area II is ~35 m), their temporal deformation patterns are alike. The largest
 deformations occurred in the summers of 2017 and 2018 for both Area I and Area II in Fig. 6b. Boxplots (Fig. 6c-d) of the
 deformation show the landslide moved much faster in summers than winters. For the east part of the landslide (Area I in Fig.
 6a), mean summer displacement rates is ~3.4 cm/d, while the mean winter displacement rates is ~2.6 cm/d (Fig. 6c). The
 highest displacement rates occur in summers of 2017 (6.74 cm/d) and 2018 (8.32 cm/d). For the west part (Area II in Fig. 6a),
 205 the mean summer and winter displacement rates are ~2 and 0 cm/d (negative values are due to uncertainties), respectively. The
 displacement rates in summers of 2017 and 2018 are 4.5 cm/d and 6.49 cm/d, respectively.

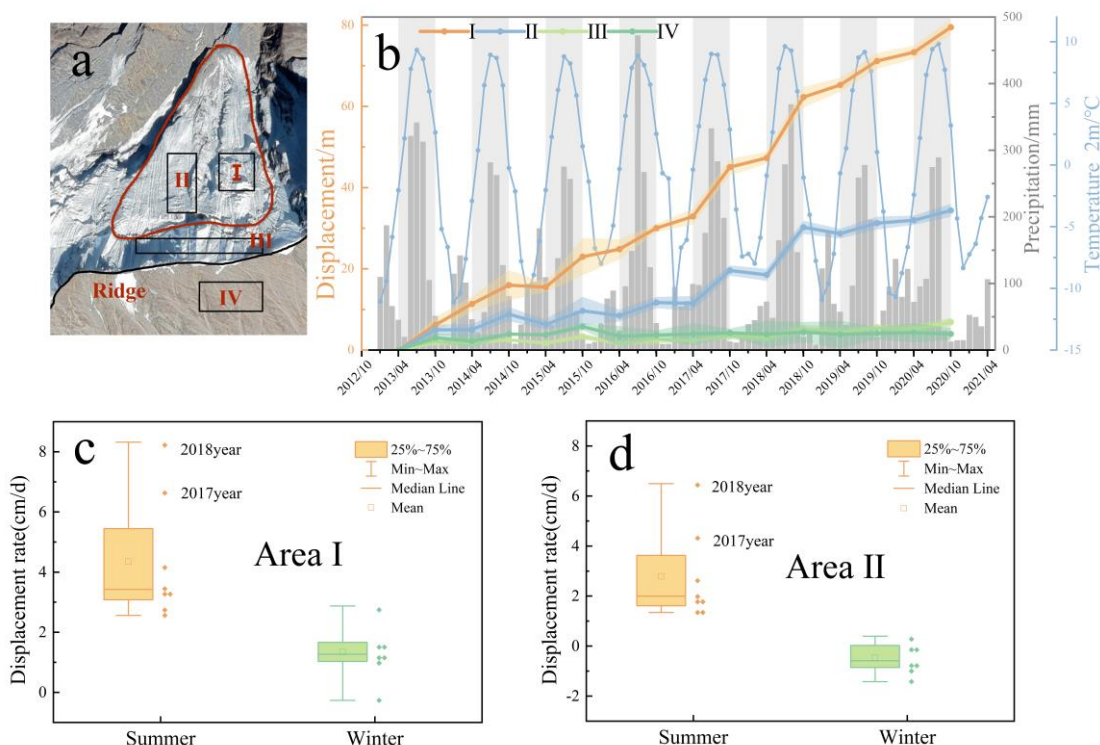


Figure 6: Four sub-areas in (a) are selected to show displacements in summers and winters of the landslide (Area I and II) and non-landslide slopes (Area III and IV) (b). Monthly precipitations (grey columns) and mean air temperatures (the blue dotted line) are

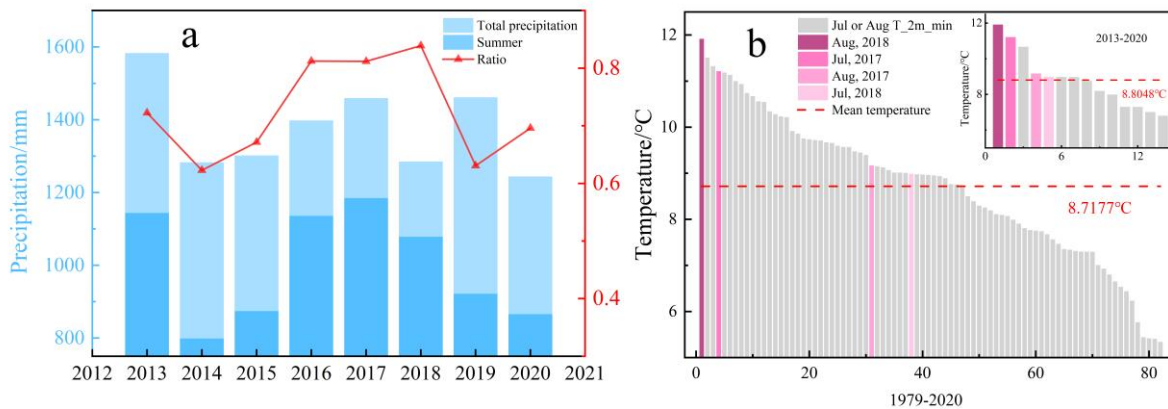


210 also shown in (b). Boxplots of summer and winter displacements of the landslide in area I and II are shown in (c) and (d), respectively. (Fig. a base map from © Google Earth 2024)

4.3 Higher temperatures and more precipitations in summers of 2017/18

Fig. 7a shows annual, summer precipitation (4.1-9.30) and its ratio to the full year precipitation from 2013 to 2020 derived from the ERA5 data. Annual precipitations in the study area are >1200 mm. Though total annual precipitations in 2017 and 215 2018 are not the highest, summer precipitation ratios of 2016-2018 are among the top three highest, with > 80% precipitation occurred in summer months. The insulator effect of the pre-summer winter snowfall cannot alone explain the accelerations in summers of 2017/2018 (as shown in Bast et al., 2024), because the summer precipitation ratio in 2018 is also very high indicating lower snowfall in the winter before the 2019 summer, which did not show significant slope acceleration.

Temperature is another possible driving factor for the landslide deformation. As the highest temperatures of the year occur in 220 the summer months of July and August, we ranked mean temperatures of July and August in 1979-2020 using ERA5 data (Fig. 7b). The August of 2018 (11.92°C, 1/82) and the July of 2017 (11.21°C, 4/82) are among the highest in 41 years. Temperatures in July 2018 and August 2017 are also greater than the 41-year mean temperature of 8.7°C. Summer temperatures in 2017 and 2018 are the top two highest months from 2013 to 2020 (inset Fig. 7b).



225 **Figure 7: Annual, summer precipitation (from April to October) and summer precipitation ratio (a) for the Chamoli landslide. Air temperatures of July and August from 1979 to 2020 sorting from largest to smallest (b). Inset (b) is summer temperature rankings from 2013 to 2020. Both precipitation and temperature data used are from the ERA5 dataset.**

5 Discussion

5.1 Improvement of the method

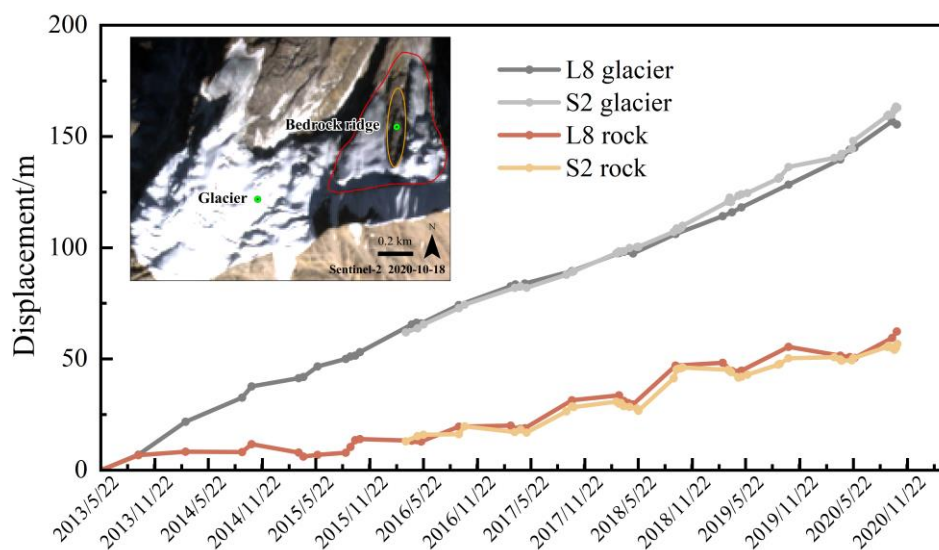
230 During POT processing, it is a routine way find a stable area to eliminate mismatches in image pairs (Bontemps et al., 2018; Lacroix et al., 2018; Yang et al., 2020). Finding a true stable area is quite challenging in complex mountain environments like the Chamoli study area, which could be the reason for the inconsistency in deformation time series between the Sentinel-2 and Landsat 8 images in Fig. 5a, Shugar et al. (2021) and Van Wyk de Vries et al. (2022). In this work, our proposed histogram-



235 based method eliminated the subjectivity in selecting a stable area and reconciled intra-annual deformations in both data
revealing the contrasting summer/winter deformation patterns in the study period. Our multi-year time-series deformation from
2013 to 2021 indicates that major deformations of the Chamoli ice-rock block occurred in summers of 2017 and 2018. Both
years have the highest summer temperatures during 1979-2021 and higher than average summer precipitations from 2013 to
2021.

5.2 Our measured deformation is the entire landslide

240 Previous works show that much part of the Chamoli landslide is covered by ice (Shugar et al., 2021; Van Wyk de Vries et al.,
2022), raising the question of whether our measured deformations are the entire landslide or the ice layer on the surface of the
landslide. Here we list two lines of evidence to support our claim that our measures are ice-rock instead of only surface ice
layer deformations. First, the deformation time series of a neighbouring glacier (Fig. 8) is linear and much larger, compared to
the nonlinear and much smaller deformation of the Chamoli landslide. As both this glacier and the landslide share similar
245 elevations, aspects, and slopes, and they are very close to each other, their deformation time series should be similar if our
measures are only surface ice layers. Second, although Shugar et al. (2021) estimated ~20 m thick surface ice layers of the
Chamoli landslide in February 2021, the surface ice layers were probably much thinner in the summer months due to
sublimation and possible partial melt at high temperatures. In fact, remote sensing images in September and October (optical
images in other summer years are mostly covered by clouds) of the landslide surface have much lower albedo than
250 neighbouring glaciers (Supplement 4). The reason for the seasonal deformation difference of the landslide (summers deform
faster than winters) is that the rock had much lower albedo, absorbed more short-wave radiance, and heated up faster compared
to the neighbouring glacier. Thus, darker rock can conduct heat underneath to reduce the strength of the ice in rock joints,
while temperatures around glaciers could remain less variable through the self-cooling effect (Salerno et al., 2023). This could
explain the contrasting cumulative deformations between the Chamoli landslide and its neighbouring glacier.



255

Figure 8: Displacement comparison of the Chamoli landslide and the neighbouring glacier. The inset image shows the location of the selected glacier and landslide points (from © Google Earth 2024).

5.3 Rising temperatures decreased ice strength on the sliding plane

Previous works (Shugar et al., 2021; Van Wyk de Vries et al., 2022) show that the detached Chamoli landslide in February 2021 are an integral block. Our results that the deformation in the east part of the Chamoli landslide is the largest (~60 m since 2013, Fig. 4e) and the deformation decreased to the north (downslope) and west parts indicates that the east part of the block has already detached from the beneath bedrock while the west and north part were still attached to the bedrock during most time of our study period. To explain the summer accelerations of the landslide, we speculate that there was underground ice on the sliding plane beneath the east part of the landslide bonding it to the bedrock. Higher than usual summer temperatures in 2017/18 decreased the cohesion strength of the ice on the sliding plane. Previous work shows that an increase of 1°C will lead to a decrease of 10% in ice strength (Mamot et al., 2018). The 2°C higher of 2017/18 summer temperatures than normal years could lead to ~20% decrease in the strength of the ice in joints. If liquid rain fell on the landslide in the exceptionally high summers of 2017/18, it may percolate deeper through fissures and pores (The crack details can be seen in Fig. 1d and Fig. S6 of Supplement 6) to increase the efficiency of the rising temperatures' impact on underground ice (Gruber and Haeberli, 2007). Raining waters are always warmer than ice-cemented slopes, infiltration of which could further decrease ice strength. In addition, infiltrated water could further decrease the friction of the ice (resisting force of the landslide), leading to accelerating deformations in summers of 2017/18. However, as we do not have in-situ measurements at the landslide with an elevation of >5000 m, phase state of summer precipitations and its role on the Chamoli landslide reserves further investigations. Significant cumulative deformations in 2017 and 2018 probably make the landslide more vulnerable and set the stage for the final collapse in February 2021, during which the landslide also experienced higher temperatures than previous years (Srivastava et al., 2022; Supplement 5). Two days before the landslide (on the 5 February 2021), scarps around the landslide

275



clearly stands out on high spatial resolution images (Supplement 6), indicating the landslide is no longer attached to the bedrock and only bonded by ice on the sliding plane (Fig. 9).

The stability of a slope can be described by the balance between two terms: the driving force (F_d) and the resisting force (F_r).

280 The driving force is mainly the gravity of the mass, while the resisting force is mainly related to cohesion and friction. The balance between these two forces is called the safety factor F_s :

$$F_s = \frac{F_r}{F_d} \quad (1).$$

When the safety factor of a slope is less than 1, the slope is considered unstable. (Das and Sivakugan, 2017)

285 The cracks in the Chamoli landslide may be > 100 meters deep, which yields a stress of ~ 3 MPa. Laboratory experiments showed that the shear strength of ice-filled joints increases linearly with the increase of normal stress and satisfies the Mohr-Coulomb criterion (Huang et al., 2023). At -15°C, the cohesion of ice is 0.69 MPa and the friction angle is 33.5°.

The Mohr–Coulomb criterion can be used to express the relationship between the shear strength and the normal stress as follows:

$$\tau_p = c_j + \sigma_n \tan \varphi_j \quad (2),$$

290 where τ_p is the shear stress on the plane, σ_n is the normal stress on the plane, c_j is the cohesion of ice-filled joints and φ_j is the internal friction angle of the ice-filled joints.

The driving force (F_d) is

$$F_d = mg \sin \alpha \quad (3),$$

and the resisting force (F_r) is

295 $F_r = \tau_p * S_p \quad (4),$

where S_p is the area of the sliding plane, α is slope angle of the valley that the landslide moved on.

For the Chamoli landslide, the driving force was constantly the component of gravity along the slope ($F_d \approx 2.95 * 10^{11} \text{N}$). A remote sensing image on February 5 (2 days before the collapse) clearly shows boundary (mainly cracks) of the triangular block, indicating that the landslide was already separated from the bedrock at that time. It was ice that bonding the landslide
300 on place and temperature rise could cause the shear strength of the ice to decrease. According to the relationship between temperature and ice strength under the normal stress of the Chamoli landslide, the strength of the ice on the sliding plane at -15°C and -8°C were $F_r \approx 6.04 * 10^{11} \text{N}$ and $F_r \approx 4.83 * 10^{11} \text{N}$, respectively (Huang et al., 2023; Mamot et al., 2018). When the temperature rise to -3°C, the shear strength (F_r) would decrease to $F_r = 2.55 * 10^{11} \sim 2.85 * 10^{11} \text{N}$, which is smaller than the sliding force of $F_d \approx 2.95 * 10^{11} \text{N}$, meaning the occurrence of the landslide.

305 Although there are many uncertainties in estimating the shear strength, such as crack opening and joint roughness, it does not affect the decreasing trend of the shear strength due to temperature rise before the Chamoli landslide.

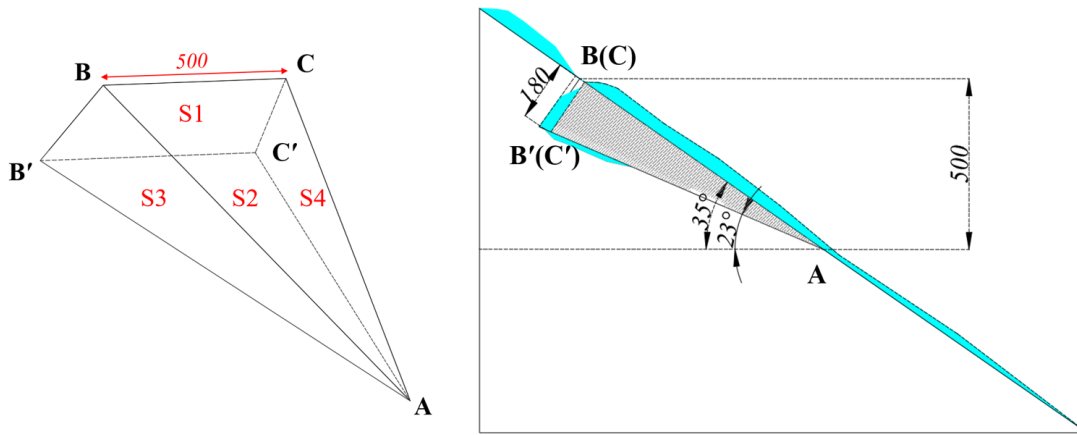


Figure 9: Schematic diagram of the Chamoli ice-rock landslide.

5.4 Evidence of the underground ice on the sliding plane

310 We argue that major ice of the Chamoli ice-rock block was on the sliding plane instead of the landslide surface, which is different to the findings of Shugar et al. (2021). Here we list two lines of evidence. First, the presence of ice beneath the sliding plane can be inferred from the speed of the avalanche that reached the bottom valley (Shugar et al., 2021) and the relative altitude (~1800 m). To reach the measured speed (114~120m/s from Shugar et al., 2021), there must be ice beneath the sliding block as a cushion to decrease the frictional strength of the block during the slide from the source area to the valley bottom.

315 The friction coefficient μ between the detached block and the beneath slope can be calculated by considering the velocity of the landslide reaching the bottom valley and the relative height it descended. During this process, the gravitational potential energy transferred to kinetic energy after the collapse by overcoming the friction between the landslide and the slope. With known descended height, the average friction coefficient can be calculated with

$$mgh = \frac{1}{2}mv_f^2 + \mu mgs \quad (5),$$

320 where h is the elevation difference from the landslide source to the bottom valley, s is the sliding distance from the landslide to the bottom valley, g is the gravitational acceleration, and v is the speed when the landslide reached the bottom valley.

Under ideal conditions, the derived friction coefficient μ from equation (5) is 0.34-0.36, which is closer to the friction coefficient of ice-rock mixture (Note the friction coefficient of rock is ~0.6, Byerlee, 1978; Beeman et al., 1988). However, there would be numerous bulges and lots of collisions along the sliding way. So, the actual μ might be even smaller and only

325 the existence of ice under the landslide block could satisfy this constrain. Second, the ice beneath the sliding block made the exceptionally long runoff distance of the disintegrated mass possible. According to the inversion of high-frequency signal (Shugar et al., 2021), the velocity of the landslide impacting the valley bottom was 114 ~120 ms^{-1} . Note this velocity is a vector that can be decomposed into two components, one that was parallel and one that was perpendicular to the valley bottom (Fig. 10a). The velocity component that was perpendicular to the valley bottom would diminish and convert to heat by clashing with



330 the bottom valley. The initial velocity of the mass at the valley bottom would be the velocity component that was parallel to the slope of the bottom valley,

$$v_i = v_0 \times \cos(\alpha - \beta) \quad (6)$$

Where v_0 is 120 ms^{-1} , β is the slope of the bottom valley (15° , measured with the ALOS 30m DEM). With this initial velocity in the bottom valley, we can calculate the maximum distances of the smashed mass that can travel.

335 $\mu mgs = \frac{1}{2}mv_i^2 + mgs \sin \beta \quad (7)$

where μ is the friction coefficient between the moving mass and the valley bottom, s is the maximum travelling distance of the mass that can travel on the valley bottom, β is the slope angle of the valley bottom. This equation estimates the longest moving distance of the moving mass by considering the initial kinetic energy (the first term to the right), the gravitational potential energy during the process (the second term to the right) and the energy consumed by friction along the path.

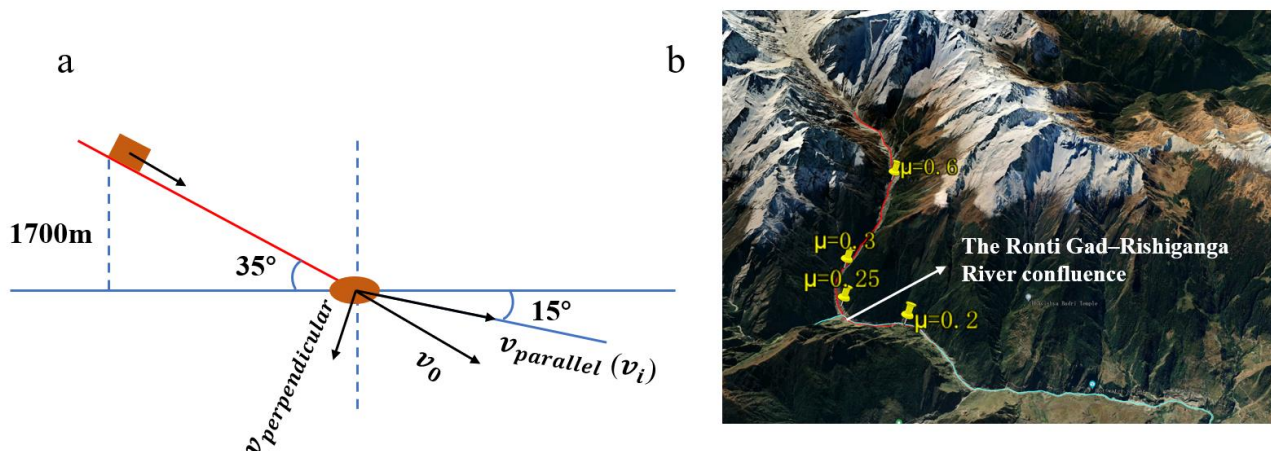
340 We consider the following hypotheses.

(1) No ice beneath the moving mass. The bottom of the moving mass would be rock or boulder. If we assume it was rock/boulder (gneiss $\mu = 0.6$) (Byerlee, 1978) beneath the mass, the maximum travel distance would be 3.4km.

(2) If there was mainly ice beneath the moving mass (with $\mu = 0.3$) (Schulson and Fortt, 2012), the maximum travel distance would be 6.8 km.

345 (3) If there was ice-water mixture beneath the moving mass (with $\mu = 0.2$) (Beeman et al., 1988), the maximum travel distance would be 10.1 km.

Above maximum travelling distances are ideal states with straight-line shaped travelling path (Fig. 10b). Actually, the shape of the valley bottom is not straight and there were collisions that could significantly attenuate velocity of the moving mass and thus significantly shorten the travelling distance. As the distance from the initial point of the block in the valley to the Ronti
350 Gad–Rishiganga River confluence is $> 8\text{km}$, the first hypotheses should be rejected meaning there was ice beneath the landslide. The initial clash of the block with the bottom valley probably melted some cushion ice, which further decreased the frictional strength of the disintegrated mass.



355 **Figure 10:** Illustration of the landslide came down along the valley slope (the red box in a) and collide with the bottom valley (the red ellipse in a). The velocity of the landslide reaching the bottom valley (v_0) can be decomposed into two components (v_i or $v_{parallel}$ and $v_{perpendicular}$). The maximum motion trajectories of the landslide block with different friction coefficients after falling into the bottom valley and runoff distances ignoring collisions with the valley wall (b) (from © Google Earth 2024).

5.5 Implications

360 Our findings have important implications for future climate change as higher elevations are disproportionately affected by global warming relating to the elevation dependent warming effect (Mountain Research Initiative EDW Working Group 2015). Rising temperature (Supplement 7) will decrease the strength of ice-cemented slopes and elongate summertime further magnifying precipitation's impact on slope instability. Ongoing climate change will dramatically increase the frequency of the Chamoli-style landslide hazards via the above recognized processes in deglaciating high mountain Asia. Future regional and slope scale landslide hazard modelling could benefit by considering above revealed processes under climate changing scenarios.

365 6 Conclusions

This work solved inconsistencies in landslide deformation time series between Landsat 8 and Sentinel-2 datasets. Reconciled measures unanimously show major deformations of the Chamoli landslide occurred in summers of 2017/18, which is closely related to extreme summer temperatures. By then, the east part of the landslide is only attached to the bedrock by ice and rising temperature decreased the strength of the ice leading to accelerations in summers and the final collapse in February 2021. This work provides rare direct observations of climate change's impact on landslides in extremely high Asian mountain regions. Future climate change will probably result in more similar landslides in deglaciating mountain regions.



CRedit authorship contribution statement

Jing Tian: Writing – initial drafting, data processing. **Wentao Yang:** Conceptualization, Writing – review & editing. **Jian Fang:** Writing – review & editing. **Chong Xu:** Writing – review & editing.

375 **Declaration of Competing interest**

The authors declare that they have no known competing financial interests or personal relationships that could have appeared to influence the work reported in this paper.

Data availability Statement

380 The Sentinel-2/Landsat 8 images were accessed from the Google Earth Engine platform at <https://earthengine.google.com>. We used COSI-Corr (Leprince et al., 2007) and Python, for the post-processing and data analysis, respectively. GPM datasets can be downloaded directly from NASA website at https://gpm1.gesdisc.eosdis.nasa.gov/data/GPM_L2/GPM_2ADPR.07. The ERA5 reanalysis data used in this study is downloaded from the Copernicus Climate Change Service (C3S) Climate Data Store (CDS) at <https://doi.org/10.24381/cds.adbb2d47> (Hersbach et al., 2023). Results of five optical POT experiments and related code can be accessed at <https://doi.org/10.6084/m9.figshare.26230901>.

385 **Acknowledgements**

This research was funded by the National Institute of Natural Hazards, Ministry of Emergency Management of China (2023-JBKY-57), the National Natural Science Foundation of China (Grant No. 42077441 & 42077259). The authors would like to show our thanks to the following colleagues: Prof. Duncan J. Quincey, Prof. Jonathan L. Carrivick and Dr. Liam Taylor from University of Leeds, Dr. Stuart Dunning from Newcastle University, Dr. Shao Sun from Chinese Academy of Meteorological Sciences, Dr. Huiran Gao from National Institute of Natural Hazards and Prof. Jidong Wu from Beijing Normal University. 390 Their discussions and suggestions played an important role in the finalisation of this paper.

References

- Beeman, M., Durham, W. B., Kirby, S. H.: Friction of ice. *Journal of Geophysical Research, Solid Earth*, 93(B7), 7625-7633., <https://doi.org/10.1029/JB093iB07p07625>, 1988.
- 395 Bhambri, R., Mehta, M., Dobhal, D. P., Gupta, A. K., Pratap, B., Kesarwani, K., Verma, A.: Devastation in the Kedarnath (Mandakini) Valley, Garhwal Himalaya, during 16–17 June 2013: a remote sensing and ground-based assessment, *Nat. Hazards*, 80, 1801-1822, <https://doi.org/10.1007/s11069-015-2033-y>, 2016.



- Biskaborn, B. K., Smith, S. L., Noetzli, J., Matthes, H., Vieira, G., Streletskiy, D. A., Lantuit, H.: Permafrost is warming at a global scale, *Nat. Commun.*, 10(1), 264, <https://doi.org/10.1038/s41467-018-08240-4>, 2019.
- 400 Bontemps, N., Lacroix, P., Doin, M. P.: Inversion of deformation fields time-series from optical images, and application to the long term kinematics of slow-moving landslides in Peru, *Remote Sens. Environ.*, 210, 144-158, <https://doi.org/10.1016/j.rse.2018.02.023>, 2018.
- Byerlee, J.: Friction of rocks. *Rock Frict, Earthq. Predict.*, 615-626, https://doi.org/10.1007/978-3-0348-7182-2_4, 1978.
- Chen, K., Avouac, J. P., Aati, S., Milliner, C., Zheng, F., Shi, C.: Cascading and pulse-like ruptures during the 2019 Ridgecrest
405 earthquakes in the Eastern California Shear Zone, *Nat. Commun.*, 11(1), 22, <https://doi.org/10.1038/s41467-019-13750-w>, 2020.
- Coe, J. A., Bessette-Kirton, E. K., Geertsema, M.: Increasing rock-avalanche size and mobility in Glacier Bay National Park and Preserve, Alaska detected from 1984 to 2016 Landsat imagery, *Landslides*, 15(3), 393-407, <https://doi.org/10.1007/s10346-017-0879-7>, 2018.
- 410 Cook, K. L., Andermann, C., Gimbert, F., Adhikari, B. R., Hovius, N.: Glacial lake outburst floods as drivers of fluvial erosion in the Himalaya, *Science*, 362(6410), 53-57, <https://doi.org/10.1126/science.aat4981>, 2018.
- Das, B. M., Sivakugan, N.: *Fundamentals of geotechnical engineering*, Cengage Learning., 2017.
- Das, L., Meher, J. K.: Drivers of climate over the Western Himalayan region of India: A review, *Earth Sci. Rev.*, 198, 102935, <https://doi.org/10.1016/j.earscirev.2019.102935>, 2019.
- 415 Deline, P., Gruber, S., Amann, F., Bodin, X., Delaloye, R., Failletaz, J.: Ice loss from glaciers and permafrost and related slope instability in high-mountain regions, *Snow Ice Relat. Hazards Risks Disasters*, (pp. 501-540), <https://doi.org/10.1016/B978-0-12-817129-5.00015-9>, 2021.
- Emberson, R., Kirschbaum, D., Stanley, T.: Global connections between El Nino and landslide impacts, *Nat. Commun.*, 12(1), 2262, <https://doi.org/10.1038/s41467-021-22398-4>, 2021.
- 420 Gruber, S., Haeberli, W.: Permafrost in steep bedrock slopes and its temperature-related destabilization following climate change, *J. Geophys. Res. Earth Surf.*, 112(F2), <https://doi.org/10.1029/2006JF000547>, 2007.
- Guo, C., Montgomery, D. R., Zhang, Y., Zhong, N., Fan, C., Wu, R.: Evidence for repeated failure of the giant Yigong landslide on the edge of the Tibetan Plateau, *Sci. Rep.*, 10(1), 14371, <https://doi.org/10.1038/s41598-020-71335-w>, 2020.
- Hersbach, H., Bell, B., Berrisford, P., Biavati, G., Horányi, A., Muñoz Sabater, J.: ERA5 hourly data on single levels from 1940
425 to present [Dataset], Copernicus Climate Change Service (C3S) Climate Data Store (CDS), <https://doi.org/10.24381/cds.adbb2d47>, 2023.
- Huang, S., Cai, H., Xin, Z., Liu, G.: The temperature-dependent shear strength of ice-filled joints in rock mass considering the effect of joint roughness, opening and shear rates, *Cryosphere*, 17(3), 1205-1223, <https://doi.org/10.5194/tc-17-1205-2023>, 2023.
- 430 Jiang, R., Zhang, L., Peng, D., He, X., He, J.: The landslide hazard chain in the Tapovan of the Himalayas on 7 February 2021, *Geophys. Res. Lett.*, 48(17), e2021GL093723, <https://doi.org/10.1029/2021GL093723>, 2021.



- Khanal, S., Tiwari, S., Lutz, A. F., Hurk, B. V. D., Immerzeel, W. W.: Historical Climate Trends over High Mountain Asia Derived from ERA5 Reanalysis Data, *J. Appl. Meteorol. Climatol.*, 62(2), 263-288, <https://doi.org/10.1175/JAMC-D-21-0045.1>, 2023.
- 435 Kirschbaum, D., Kapnick, S. B., Stanley, T., Pascale, S.: Changes in extreme precipitation and landslides over High Mountain Asia, *Geophys. Res. Lett.*, 47(4), <https://doi.org/10.1029/2019GL085347>, 2020.
- Lacroix, P., Belart, J. M., Berthier, E., Sæmundsson, Þ., Jónsdóttir, K.: Mechanisms of landslide destabilization induced by glacier-retreat on Tungnakvísarljökull area, Iceland, *Geophys. Res. Lett.*, 49(14), <https://doi.org/10.1029/2022GL098302>, 2022.
- 440 Lacroix, P., Bièvre, G., Pathier, E., Kniess, U., Jongmans, D.: Use of Sentinel-2 images for the detection of precursory motions before landslide failures, *Remote Sens. Environ.*, 215, 507-516, <https://doi.org/10.1016/j.rse.2018.03.042>, 2018.
- Larsen, I. J., Montgomery, D. R.: Landslide erosion coupled to tectonics and river incision, *Nat. Geoscience*, 5(7), 468-473. <https://doi.org/10.1038/ngeo1479>, 2012.
- Leprince, S., Ayoub, F., Klingler, Y., Avouac, J. P.: Co-registration of optically sensed images and correlation (COSI-Corr):
445 An operational methodology for ground deformation measurements, *IEEE IGARSS 2007*, 1943-1946, <https://doi.org/10.1109/IGARSS.2007.4423207>, 2007.
- Lewkowicz, A. G., Way, R. G.: Extremes of summer climate trigger thousands of thermokarst landslides in a High Arctic environment, *Nat. Commun.*, 10(1), 1329, <https://doi.org/10.1038/s41467-019-09314-7>, 2019.
- Li, X., Handwerker, A. L., Peltzer, G., Fielding, E.: Exploring the Behaviors of Initiated Progressive Failure and Slow-Moving
450 Landslides in Los Angeles Using Satellite InSAR and Pixel Offset Tracking, *Geophys. Res. Lett.*, 51(13), <https://doi.org/10.1029/2024GL108267>, 2024.
- Mamot, P., Weber, S., Schröder, T., Krautblatter, M.: A temperature-and stress-controlled failure criterion for ice-filled permafrost rock joints, *Cryosphere*, 12(10), 3333-3353, <https://doi.org/10.5194/tc-12-3333-2018>, 2018.
- McCull, S. T.: Paraglacial rock-slope stability, *Geomorphology*, 153, 1-16, <https://doi.org/10.1016/j.geomorph.2012.02.015>,
455 2012.
- Michel, S., Avouac, J. P., Ayoub, F., Ewing, R. C., Vriend, N., Heggy, E.: Comparing dune migration measured from remote sensing with sand flux prediction based on weather data and model, a test case in Qatar, *Earth Planet. Sci. Lett.*, 497, 12-21, <https://doi.org/10.1016/j.epsl.2018.05.037>, 2018.
- Miles, B. W., Jordan, J. R., Stokes, C. R., Jamieson, S. S., Gudmundsson, G. H., Jenkins, A.: Recent acceleration of Denman
460 Glacier (1972–2017), East Antarctica, driven by grounding line retreat and changes in ice tongue configuration, *Cryosphere*, 15(2), 663-676, <https://doi.org/10.5194/tc-15-663-2021>, 2021.
- Mountain Research Initiative EDW Working Group.: Elevation-dependent warming in mountain regions of the world, *Nat. Clim. Chang*, 5(5): 424-430, <https://doi.org/10.1038/nclimate2563>, 2015.
- Pei, Y., Qiu, H., Yang, D., Liu, Z., Ma, S., Li, J.: Increasing landslide activity in the Taxkorgan River Basin (eastern Pamirs
465 Plateau, China) driven by climate change, *Catena*, 223, 106911, <https://doi.org/10.1016/j.catena.2023.106911>, 2023.



- Qi, W., Yang, W., He, X., Xu, C.: Detecting Chamoli landslide precursors in the southern Himalayas using remote sensing data, *Landslides*, 18(10), 3449-3456, <https://doi.org/10.1007/s10346-021-01753-y>, 2021.
- Sæmundsson, Þ., Morino, C., Helgason, J. K., Conway, S. J., Pétursson, H. G.: The triggering factors of the Móafellshyrna debris slide in northern Iceland: Intense precipitation, earthquake activity and thawing of mountain permafrost, *Sci. Total Environ.*, 621, 1163-1175, <https://doi.org/10.1016/j.scitotenv.2017.10.111>, 2018.
- 470 Sahoo, P. K., Kumar, S., Singh, R. P.: Neotectonic study of Ganga and Yamuna tear faults, NW Himalaya, using remote sensing and GIS, *Int. J. Remote Sens.*, 21(3), 499-518, <https://doi.org/10.1080/014311600210713>, 2000.
- Salerno, F., Guyennon, N., Yang, K., Shaw, T. E., Lin, C., Colombo, N.: Local cooling and drying induced by Himalayan glaciers under global warming, *Nat. Geoscience*, 16(12), 1120-1127, <https://doi.org/10.1038/s41561-023-01331-y>, 2023.
- 475 Schulson, E. M., Fortt, A. L.: Friction of ice on ice. *Journal of Geophysical Research: Solid Earth*, 117(B12), <https://doi.org/10.1029/2012JB009219>, 2012.
- Shrestha, A. B., Steiner, J., Nepal, S., Maharjan, S. B., Jackson, M., Rasul, G., Bajracharya, B.: Understanding the Chamoli flood: Cause, process, impacts, and context of rapid infrastructure development. *River Basins and Cryosphere*, ICIMOD, Kathmandu, Nepal, 2021.
- 480 Shugar, D. H., Jacquemart, M., Shean, D., Bhushan, S., Upadhyay, K., Sattar, A.: A massive rock and ice avalanche caused the 2021 disaster at Chamoli, Indian Himalaya, *Science*, 373(6552), 300-306, <https://doi.org/10.1126/science.abh4455>, 2021.
- Skofronick-Jackson, G., Petersen, W. A., Berg, W., Kidd, C., Stocker, E. F., Kirschbaum, D. B.: The Global Precipitation Measurement (GPM) mission for science and society, *Bull. Am. Meteorol. Soc.*, 98(8), 1679-1695, <https://doi.org/10.1175/BAMS-D-15-00306.1>, 2017.
- 485 Smith, S. L., O'Neill, H. B., Isaksen, K., Noetzi, J., Romanovsky, V. E.: The changing thermal state of permafrost. *Nat. Rev. Earth Environ.*, 3(1), 10-23, <https://doi.org/10.1038/s43017-021-00240-1>, 2022.
- Srivastava, P., Namdev, P., Singh, P. K.: 7 February Chamoli (Uttarakhand, India) rock-ice avalanche disaster: model-simulated prevailing meteorological conditions, *Atmosphere*, 13(2), 267, <https://doi.org/10.3390/atmos13020267>, 2022.
- Valdiya, K. S., Goel, O. P.: Lithological subdivision and petrology of the Great Himalayan Vaikrita group in Kumaun, India, *Proc. Indian Acad. Sci. Earth Planet. Sci.*, 92, 141-163, <https://doi.org/10.1007/BF02866736>, 1983.
- 490 Van Wyk de Vries, M., Bhushan, S., Jacquemart, M., Deschamps-Berger, C., Berthier, E., Gascoin, S.: Pre-collapse motion of the February 2021 Chamoli rock-ice avalanche, *Indian Himalaya, Nat. Hazards Earth Syst. Sci.*, 22(10), 3309-3327, <https://doi.org/10.5194/nhess-22-3309-2022>, 2022.
- Yang, W.: Selecting the best image pairs to measure slope deformation, *Sensors*, 20(17), 4721, <https://doi.org/10.3390/s20174721>, 2020.
- 495 Yang, W., Liu, L., Shi, P.: Detecting precursors of an imminent landslide along the Jinsha River, *Nat. Hazards Earth Syst. Sci.*, 20(11), 3215-3224, <https://doi.org/10.5194/nhess-20-3215-2020>, 2020a.
- Yang, W., Wang, Y., Wang, Y., Ma, C., Ma, Y.: Retrospective deformation of the Baige landslide using optical remote sensing images, *Landslides*, 17, 659-668, <https://doi.org/10.1007/s10346-019-01311-7>, 2020b.

<https://doi.org/10.5194/egusphere-2024-2786>

Preprint. Discussion started: 14 October 2024

© Author(s) 2024. CC BY 4.0 License.



500 Zhang, D., Yang, W., Xu, C., Ye, T., Liu, Q.: Extracting deforming landslides from time-series Sentinel-2 imagery, *Landslides*, 19(11), 2761-2774, <https://doi.org/10.1007/s10346-022-01949-w>, 2022.